$SrTiO_3(100)/(LaMnO_3)_m(SrMnO_3)_n$ layered heterostructures: A combined EELS and TEM study

J. Verbeeck, O. I. Lebedev, and G. Van Tendeloo
EMAT, University of Antwerp (RUCA), Groenenborgerlaan 171, B-2020 Antwerp, Belgium

B. Mercey
Laboratoire CRISMAT, ISMRA, UMR 6508,Université de Caen, 6 Bd. du Maréchal Juin, 14050 Caen Cedex, France
(Received 13 June 2002; published 26 November 2002)

Epitaxially grown heterostructures consisting of alternating layers of $LaMnO_3$ (LMO, 9 or 15 unit cells) and $SrMnO_3$ (SMO, 4 or 6 unit cells) on a $SrTiO_3(100)$ (STO(100)) substrate have been studied by a combination of high resolution transmission electron microscopy (HRTEM), electron diffraction, quantitative electron energy loss spectroscopy (EELS) with model fitting, energy filtered TEM (EFTEM) and imaging spectroscopy on an atomic scale. The combination of these techniques is necessary for the structural, chemical, and electronic characterization of these heterostructures. A model is proposed containing chemically and structurally sharp interfaces. The $SrMnO_3$ layers are stabilized in a $Pm3m$ structure between two LMO layers. Tensile stress causes oxygen deficiency in the SMO layers increasing the number of $3d$ electrons on the Mn sites to resemble the Mn^{3+} sites in LMO. The energy loss near edge structure (ELNES) of O and Mn is compared for both LMO and SMO layers and shows that the Mn-O bonds have a partially covalent character. The absence of a strong valency effect in the Mn ELNES is due to the oxygen vacancies in SMO.

DOI: 10.1103/PhysRevB.66.184426 PACS number(s): 75.30.Vn, 73.21.Ac, 79.20.Uv

I. INTRODUCTION

Doped manganite perovskites of the type $A_{1-x}A'_xMnO_3$ (A trivalent cation, A' divalent cation) exhibit interesting properties like colossal magnetoresistance (CMR) and metal-to-insulator transitions, depending on the doping level x. [1] It is assumed that doping $AMnO_3$ compounds with divalent A' cations changes the valency of Mn from Mn^{3+} to a mixed Mn^{4+}/Mn^{3+} state, hence these materials are called controlled valency materials. This mixed valency was found crucial for the explanation of the coupling of ferromagnetic order with increased conductivity by the double exchange mechanism. [2] However, several papers have argued against this naive ionic picture and they point out that the Mn-O bonds in these materials have a considerable covalent character and the introduction of holes by divalent doping actually leads to holes with mixed O $2p$ - Mn $3d$ character in bulk $La_{1-x}Sr_xMnO_3$. [3–7] Further complication is introduced by the possibility of O deficiency in these materials, which changes the general formula to $A_{1-x}A'_xMnO_{3-\delta}$.

Experimental studies on perovskite based bulk materials of the type $(A,A')MnO_3$ have shown that three parameters mainly control the magnetic and electronic properties: (a) the valence of the manganese which is determined by the ratio between the divalent and the trivalent cations, (b) the average A-site cationic radius, and (c) the difference in size between both A-site cations. [8–10] It was found that introducing A-site ordering increases the Curie temperature and the metal-insulator transition temperature in bulk $LaBaMn_2O_6$ as compared to the disordered phase. [11] However, such an ordered bulk material is difficult to synthesize using the classical solid state synthesis methods.

Thin film laser molecular beam epitaxy (laser-MBE) growth methods offer the possibility, utilizing a multi-target deposition process, to directly control the location of the different cations in an artificial superlattice. Creating this artificial superlattice allows the verification of the assumptions about the valency and the study of the electronic localization of the introduced holes. One could imagine that introducing a spatial separation of the Sr doping in $La_{1-x}Sr_xMnO_3$ could lead to interesting new properties by keeping the lattice order high, while still adding extra holes to the system. This artificial A-site ordering allows use to test some ideas about mixed valency materials, since a nominal valency modulation is artificially introduced.

In the present contribution, two superlattices are grown in a reflective high energy electron diffraction (RHEED) monitored laser-MBE system from two targets, $LaMnO_3$ (LMO) and $SrMnO_3$ (SMO), with a nominal average composition close to $La_{0.66}Sr_{0.33}MnO_3$ and a nominal sequence LMO_mSMO_n. The possibility to obtain information on the electronic structure of a material by using a combination of scanning transmission electron microscopy (STEM) and EELS on an atomic scale has already been shown for different materials. [12–18] Combining this technique with fitting methods to interpret the spectra gives an opportunity to investigate the chemistry of the present heterostructures on a unit cell scale. The detailed shape of the spectra contains information on the electronic structure, especially interesting in view of the valency assumptions. Energy filtered transmission electron microscopy (EFTEM) combines spectroscopic data with spatial information, enabling elemental distribution maps of the chemically modulated layers. The imaging spectroscopy technique takes EFTEM a step further and enables the spatially resolved acquisition of EELS fine structure spectra. Combining these spectroscopic techniques with more conventional techniques such as high resolution transmission electron microscopy (HRTEM) and electron diffraction (ED) enables us to complement and compare the EELS data with structural and contrast information. We show in this section, that this wide range of techniques leads to a

 ©2002 The American Physical Society

narrowing of the field of interpretation, closing in on the complex structural, chemical, and electronic reality in these samples.

II. EXPERIMENT

Two samples with nominal formula $SrTiO_3(100)/[(LaMnO_3)_{15}]_7[(SrMnO_3)_6]_6$ and $SrTiO_3(100)/[(LaMnO_3)_9]_9[(SrMnO_3)_4)]_9$ were prepared and will be indicated as LMO15SMO6 and LMO9SMO4 correspondingly. The average composition of both samples is close to $La_{0.66}Sr_{0.33}MnO_3$, a composition for which bulk LSMO shows interesting properties. [19] Dense ceramic targets with the nominal formulas $LaMnO_3$ and $SrMnO_3$ were prepared using standard ceramic synthesis methods. Appropriate ratios of La_2O_3, $SrCO_3$ and MnO_2 powders were mixed and intimately ground using a semi-planetary ball mill. The powder was annealed twice at 900 °C for 12h and once at 1200 °C for 12 h, with intermediate grinding. Pellets with a diameter of 25 mm were uniaxially cold-pressed and sintered at 1500 °C for 24 h. [20,21]

A RHEED-monitored laser-MBE system, which allows for reflection high energy electron diffraction (RHEED) monitoring of the growth has been used and was described elsewhere. [22] Briefly, the base pressure is very low (10^{-6} Pa) and the deposition is carried out in a pressure typically ranging between 10^{-2} and 5×10^{-2} Pa. The UV beam ($\lambda=248$ nm, repetition rate 2 Hz) from an excimer laser is focused onto the sintered target to obtain an energy density ranging between 10^{-4} and 2×10^{-4} J/m^2. Optical quality single-crystal substrates of $SrTiO_3$ (100) were ultrasonically cleaned in acetone and in alcohol. To obtain a flat and terraced surface, the substrate, which has no intentional cut-off angle, is etched in a buffered NH_4F/HF solution. [23] This etching provides large and flat surfaces and smooth interfaces are obtained when a Stranki-Krastanov growth mode is stabilized. This growth mode allows for the observation of the RHEED oscillations.

To improve the quality of the surface, prior to the deposition of the superlattice, the substrate is buffered with 24 layers of $SrTiO_3$ deposited at 720 °C in a dynamic vacuum of 1.5×10^{-2} Pa of molecular oxygen. Care has been taken to ensure that the STO substrate ends with a SrO layer by using a Sr_2TiO_4 target for the last two layers. During the deposition of the superlattice, the heater was held at constant temperature (535 °C) in a dynamic vacuum of 5×10^{-2} Pa. To ensure a complete oxidation of the superlattice the deposition is carried out in a mixture of 94% oxygen and 6% ozone. After deposition, the superlattice is cooled to 300 °C in the same pressure and atmosphere conditions as used during the growth. Between 300 °C and 200 °C, ozone production is stopped but the pressure is held constant. Below 200 °C the superlattice is cooled in low pressure ($<5\times10^{-5}$ Pa). RHEED is used to monitor the surface stability during the cooling. Growth and magnetoresistive properties of very similar samples (nominal Sr/La content of 0.26 instead of 0.33 in our case) are described by Salvador *et al.* [20] They find a decrease in T_c, maximum MR value, and low temperature conductivity for increasing thickness of the layers in the heterostructures.

The samples described here, are comparable with samples III and IV in Ref. [20]. The magnetization of these superlattices slowly increases for $T<180$ K to reach a value around 0.7 μB/Mn. The hysteresis cycle registered at 10 K shows a high coercivity ($=700$ G) higher than that observed for the corresponding bulk material ($=5$ G). The physical properties of these two samples are not very interesting from a technological point of view, but they were selected from a set of samples since the estimated resolution of the EFTEM technique is about 1 nm. This implied the growth of at least 4 perovskite-like layers $0.39\times4=1.56$ nm. So, $n=4$ and $n=6$ were chosen as target values for the thickness of the SMO layers. It will be shown in this study that the reason for the poor physical properties is related to oxygen deficiency in the SMO layers.

Sample preparation for TEM and HRTEM was done using a standard TEM cross-section technique. Because of different ion milling effects on STO, LMO and SMO, a cross-section sample for STEM was prepared using mechanical wedge polishing.

Cross-section high resolution TEM (HRTEM) images were recorded on a JEOL 4000EX operating at 400 keV and having a point resolution of 0.17 nm. For STEM EELS experiments, use was made of the Cornell VG HB501A STEM operating at 100 keV with a cold field emission electron gun having a probe diameter of 0.2 nm and an energy spread of 0.6 eV. [24]

Each EELS spectrum is recorded by automatically scanning the STEM probe over a region of 15.7 nm, parallel to the layers to average out possible interface roughness or surface contamination. The probe is manually repositioned after each acquisition to consecutively capture data in different perpendicular positions of the layers. A total set of 36 spectra contains information starting from the bottom of LMO layer 4 going through SMO layer 4 and ending at the top of LMO layer 5. EELS spectra are collected in four different energy ranges: the low loss (-60.2–241.6 eV), the Mn $L_{2,3}$ and O K (439.7–741.6 eV), the La $M_{4,5}$ (739.7–1041.6 eV) and the Sr $L_{2,3}$ range (1839.7–2141.6 eV). Recorded spectra are analyzed using a spectrum fitting technique. All edges are fitted to an experimental reference edge from the same sample.

The fitted edge intensities serve as an estimation of the local chemical concentration with an estimated error of 10%. The STEM probe is calculated to spread from 0.2 nm at the entrance plane to around 0.32 nm at the exit plane of the specimen (diameter containing 80% intensity, thickness 25 nm, multislice simulation), which gives an indication on the expected blurring of the chemical profiles caused by electron scattering. The error on the probe position is of the order of 0.2 nm. Energy loss near edge spectroscopy (ELNES) gives information on the site and symmetry projected unoccupied density of states near the Fermi level and is performed to gain insight in the electronic structure of the material. Two edges are studied in detail: the O K-edge at (502.2–590.8 eV) and the Mn L2,3 edge (622.2–710.8 eV), both at a 30-s exposure time. Careful inspection of the spectra over time, shows no changes in the ELNES spectra at exposure times

up to 120 s. This is taken as an indication that no significant beam damage effects occur during the acquisition of the ELNES spectra.

The spectral data are treated with a standard background removal method and the high frequency noise is removed by convolution with a Gaussian profile of 0.3 eV full width at half maximum. Two spectra represent the middle part of a LMO and SMO layer. The energy resolution of this experiment is estimated around 0.65 eV by a Lorenz fit to the experimental zero loss peak. Energy filtered TEM images are recorded on a Phillips CM30 FEG equipped with a GIF 200 post column energy filter. The collection angle is approximately 19.2 mrad. Elemental maps are calculated by subtracting the non-specific background from the element-specific signal using the standard three-window technique. [25] Drift between images is corrected using a cross correlation technique.

The technique of imaging spectroscopy [26] is used to collect spatial and spectral information with a set of 99 EFTEM images starting from 500 eV with a slit width and step size of 2 eV. The exposure time was 10 s for each image of 128 $\times 128$ pixels. Drift is removed by shifting the images with respect to each other after acquisition. The resulting three-dimensional data set is reduced by integrating 100 pixels parallel to the layers, this leaves a 2 dimensional set containing EELS spectra as a function of the position perpendicular to the layers. The background under the O *K* edge is removed with a standard least mean square procedure and the resulting edge is normalized to the maximum peak height. For cosmetic reasons, a 4 point interpolation in the energy dimension is performed.

III. STRUCTURAL CONSIDERATIONS

The room temperature structure of the $SrTiO_3$ substrate is well established; it is a cubic perovskite $Pm3m$ with lattice parameter $a_{STO}=0.39050$ nm. [27]

The structure and the phases of La-Mn-O have been the subject of many investigations. The crystal structure of $LaMnO_3$ is derived from the cubic perovskite type structure; it contains Mn atoms in the octahedral sites of the oxygen sublattice, creating Mn-O-Mn bonds forming angles deviating somewhat from 180°. However, the real structure of La-Mn-O is much more complicated and strongly depends on oxygen stoichiometry, cation deficiency, ratio between Mn^{3+} and Mn^{4+}. Rotations of the MnO_6 octahedra lead to a lowering of the crystal symmetry from cubic to, e.g., orthorhombic or rhombohedral. [28–31] The different bulk phases are discussed in the literature but most research groups refer to the two main structures: the rhombohedral ($R\bar{3}c$) and the orthorhombic ($Pnma$) phases . The orthorhombic $Pnma(62)$ phase has been found for stoichiometric $LaMnO_3$ Refs. 32–34 with lattice parameters $a=5.582(0)$ Å, $b=5.583(0)$ Å, $c=7.890(0)$ Å. The non-stoichiometric La-Mn-O compound can have an oxygen excess $LaMnO_{3+\delta}$ or cation deficiency $La_{1-x}Mn_{1-y}O_3$; both of them show rhombohedral symmetry $R\bar{3}c(167)$ with $a=5.535(0)$ Å, $c=13.344$ Å.[34–38] Moreover, Maignan *et al.* reported a $La_{0.9}MnO_{3-\delta}$ phase with monoclinic symmetry $I2/a$ with $a=7.790(1)$ Å, $b=5.526(1)$ Å, $c=5.479(1)$ Å, $\alpha=90.78°$.[39]

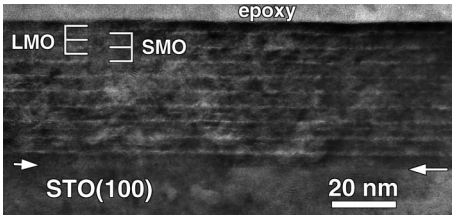

FIG. 1. Low magnification image of the LMO9SMO4 sample. The SMO layers are clearly visible as 9 brighter layers. The arrows indicate the substrate-film interface.

Stoichiometric $SrMnO_3$ has two polymorphic forms: cubic and hexagonal. The cubic structure is $Pm3m(221)$ with $a=3.805$ Å (Ref. 40) and the hexagonal one is $P6_3/mmc$ with $a=5.449$ Å and $c=9.0804$ Å. [41] Negas *et al.* [41] reported that heating $SrMnO_3$ in air at 1525°C induces oxygen deficiency ($SrMnO_{2.69}$) causing a symmetry breakdown to orthorhombic.

Both LMO and SMO are present in the heterostructures and misfit stress resulting in strain is expected. Assuming the bulk structures for SMO as well as LMO, the SMO layers are expected to be under tensile stress while the LMO will be under compressive stress.

IV. RESULTS AND DISCUSSION

A. TEM

A cross-section low magnification image of the LMO9SMO4 superlattice film is shown in Fig. 1. The film is epitaxial and exhibits sharp, flat, and well-defined interfaces between successive LMO and SMO layers. The layers can be easily distinguished due to different contrast, induced by different electron scattering and consequently a different composition of the layers. Bright bands correspond to the SMO layers and dark thicker bands correspond to the LMO layers.

Relevant information concerning the epitaxial relationship, quality, and crystal structure of the layers is obtained from the electron diffraction (ED) patterns (Fig. 2), which is a superposition of the diffraction patterns from LMO, SMO and the STO substrate. The white square indicates the positions of the LMO reflections. They can be indexed in a pseudocubic or a rhombohedral ($R\bar{3}c$) structure. No spots due to the possible presence of the orthorhombic phase are observed. The exact symmetry close to the interfaces is difficult to measure and small distortions from the nominal space groups can occur. The perfect ED pattern confirms the epitaxial growth of the layers. Moreover, the satellite spots, due to the periodic stacking of the LMO-SMO layers, are clearly visible. For the LMO15SMO6 specimen the periodicity is ≈ 82 Å. The LMO9SMO4 superlattice film exhibits the same structure perfection but the superperiod is ≈ 50 Å [Fig. 2(b)].

A cross-section HREM image of the first layers of LMO9SMO4, grown on the STO substrate is shown in Fig. 3. The first LMO buffer layer shows perfect epitaxy across

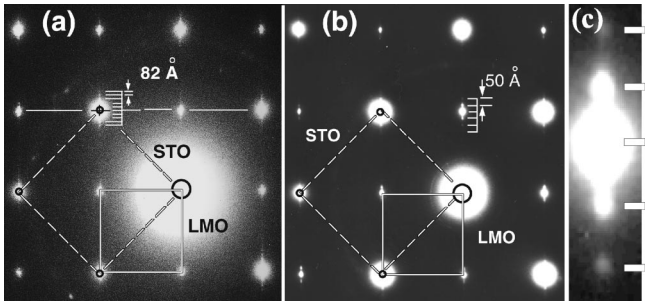

FIG. 2. Electron diffraction pattern images for LMO15SMO6 (a) and LMO9SMO4 (b) along the [001] direction of the STO substrate. The satellite spots due to long range order of the layers are indicated by the fork pattern. An enlarged satellite spot pattern from (b) is shown in (c). The full and dashed squares in (a) and (b) indicate, respectively, which spots are originating from STO and LMO.

the interface, with no secondary phase or amorphous layer present along the interface. No interface dislocations, resulting from misfit accommodation, are seen at the STO/LMO interface. The first SMO layer grows on a flat LMO surface and exhibits a sharp heteroepitaxial LMO/SMO interface. Only occasionally a perovskite unit cell step is present at the LMO/SMO interface. Surprisingly, misfit dislocations along the interface are absent although the misfit LMO-SMO for fully oxidized material would be 2.6%. This implies that the SMO perovskite-type layer is stabilized between two LMO layers and, actually, adopts the pseudo-cubic structure of LMO. In this respect it is clear that the SMO layer is under high tensile stress.

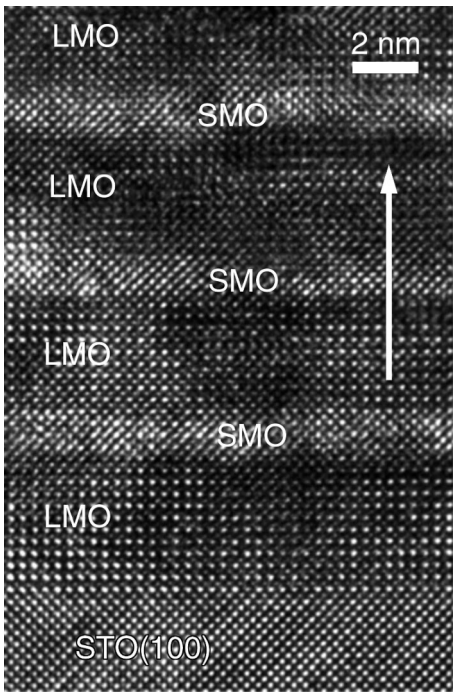

FIG. 3. HRTEM cross-section image of the LMO9SMO4 sample, the arrow indicates the direction and extent of the STEM scan for EELS analysis.

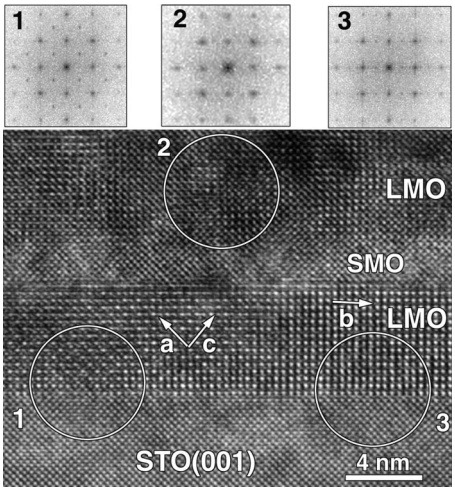

FIG. 4. HRTEM cross-section image of the LMO15SMO6 sample showing the first two LMO layers on the STO substrate. Fourier transforms are made from selected regions. The first layer (regions 1 and 3) indicate an orthorhombic symmetry, while further layers (region 2) show a pattern consistent with rhombohedral symmetry.

The cross-section HREM image of a LMO15SMO6 film (Fig. 4) is very similar to that obtained for LMO9SMO4. However, the first LMO layer shows unambiguously features of orthorhombic symmetry. Discrete Fourier transformations (FT) made from different areas of the image of the LMO/STO interface show typical spot arrangements for [010] and [110] orthorhombic zones. Nevertheless, the following LMO layers exhibit a FT pattern which is consistent with a rhombohedral structure. Again, small distortions can occur near the interfaces.

A HREM image of the interface between the STO substrate and the first LMO layer is shown at higher magnification in Fig. 5. Film and substrate are perfectly coherent.

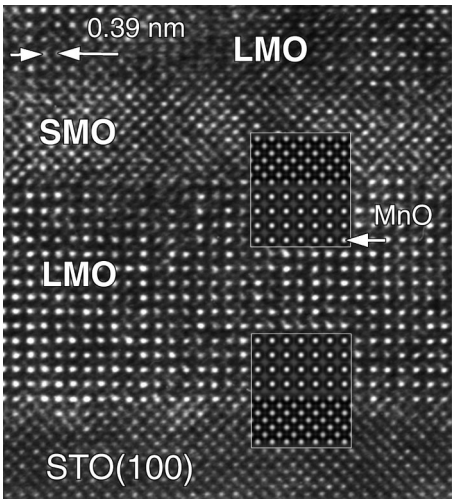

FIG. 5. HRTEM cross-section image of the (LMO15SMO6)6 sample near the substrate interface. Insets show the result of a multislice calculation for a given thickness and focus assuming a $R\bar{3}c$ symmetry for the LMO layer and $Pm3m$ for STO and SMO layers.

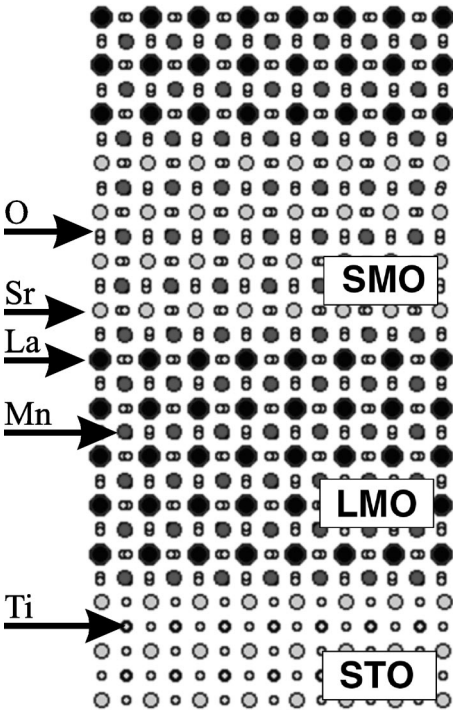

FIG. 6. Structure model of the heterostructure.

Since the crystal structures of STO and LMO are very similar (both perovskite type structures) it is reasonable to assume that the LMO layer starts to grow so as to continue the substrate structure as much as possible. Under the experimental defocus conditions and according to multislice image simulations (Fig. 5 insets), all heavy-atom columns in the STO substrate are imaged as bright dots. In the LMO image the brightest dots represent MnO columns. Since the column-projected potential of Sr and Ti-O columns is very similar, no difference in dot brightness between Sr and Ti-O columns can be discerned according to the simulations. The SMO layers also have similar Sr and Mn-O column potentials and show an intensity distribution comparable to STO. Since we prepared STO to have a SrO terminated layer (see experiment), the following layer sequence, based on this assumption and on the HREM evidence is most likely: (substrate)-TiO_2-SrO-MnO_2-LaO-(LMO layer). The cross-section HREM image of Fig. 5 reveals sharp and well-defined LMO/SMO interfaces.

The HREM images of Figs. 3 and 4 clearly indicate that, across the interface, the brightest dot rows of the LMO layers are in phase within the whole heterostructure film. This observation strongly suggests, that across the interface, the La sublattice of one LMO layer is in register with the La sublattice of following LMO layers and the Mn lattice is continuous across the whole film. Therefore, the stacking sequence at the LMO/SMO and SMO/LMO interfaces should be identical and the following layer sequence, shown in Fig. 6, is most likely: (substrate)-TiO_2-SrO-MnO_2-LaO-(LMO layer)- LaO-MnO_2-SrO-MnO_2. This sequence is maintained in all areas of the film and holds for the LMO/SMO as well as for the SMO/LMO interface. The image simulations of upper and lower interfaces in Fig. 5 are based on the rhombohedral ($R\bar{3}c$) structure for LMO (only the first LMO layer was found to be orthorhombic), cubic ($Pm3m$) structure for SMO and on the model of Fig. 6. These observations further allow us to conclude that both LMO and SMO layers show a layer by layer growth with only unit cell height steps.

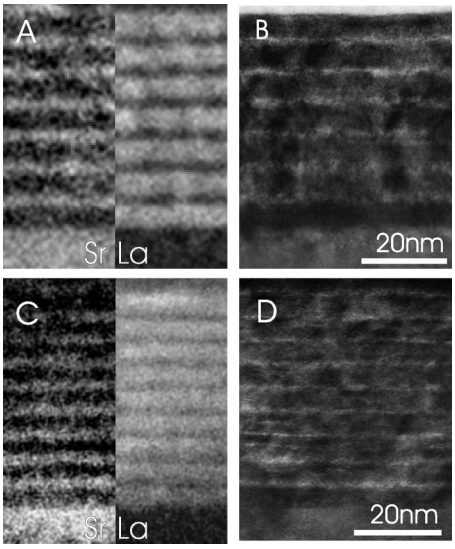

FIG. 7. Sr and La elemental maps side by side (a),(c) and conventional TEM images (b),(d) for both samples (a),(b) LMO15SMO6, (c),(d) LMO9SMO4).

Plan view specimens are studied by HRTEM and ED patterns and confirm the perfect epitaxial growth in the *ab* plane.

B. EFTEM

In view of a possible La-Sr interdiffusion leading to $La_{1-x}Sr_xMnO_3$ compounds, EFTEM analysis is performed to map the spatial distribution of chemical elements in the heterostructure. Figure 7 shows a combination of chemical maps for La and Sr (a),(c) together with the conventional TEM images (b),(d) for the two samples (a),(b): LMO15SMO6, (c),(d): LMO9SMO4). This picture shows that artificial *A*-site ordering is achieved and that no significant chemical diffusion or local concentration variation is present in the layers. The spatial resolution in the EFTEM images can be theoretically estimated by taking into account chromatic and spherical aberration as well as delocalization. This gives an estimated resolution better than 1 nm for all elements with the chosen operational parameters. Due to long exposure times, significant drift can occur, and this will deteriorate spatial resolution. Spatial resolution in EFTEM images was defined by Berger *et al.* [42] as the diameter of a disc containing 59% of the point spread function, which models the imaging of a pointlike atom taking into account the inelastic scattering and the propagation of the inelastic image through the microscope lenses. This means that with a theoretical resolution of 1 nm we cannot answer questions regarding interdiffusion of elements between layers having thicknesses comparable to this resolution. An assumed mathematical rectangular chemical profile would require frequency components up to infinity in the EFTEM image to

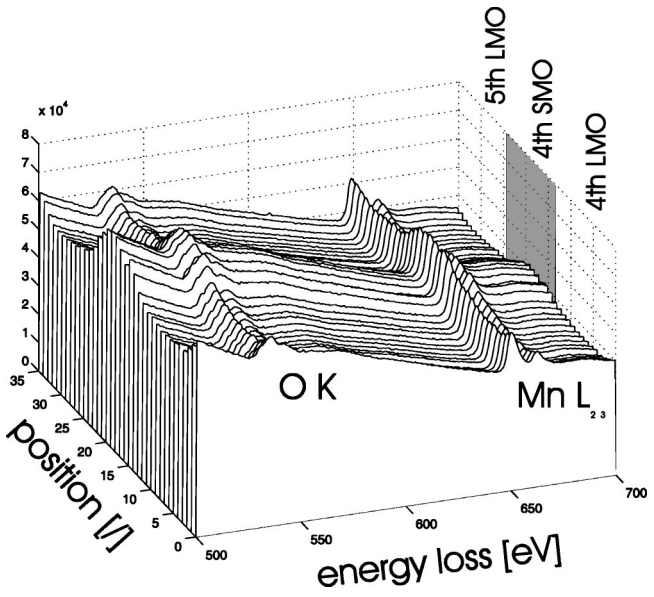

FIG. 8. EELS spectra for different positions of the STEM probe between the fourth and fifth LMO layer. O *K* and Mn *L*2,3 edges are clearly visible.

represent the profile without broadening. Saying that EFTEM has a resolution limit of 1 nm in this case, only means that we can *see* the layers as well separated, but not that we can determine the specific shape of the diffusion profile directly from the EFTEM images.

C. STEM EELS

The result of the acquisition of EELS spectra of the LMO9SMO4 sample from a position inside the fourth LMO layer to a position in the fifth LMO layer is presented in Fig. 8. The O *K* edge around 530 eV and the Mn $L_{2,3}$ edge around 640 eV are clearly visible, together with the variation of the background for different positions. On top of this dataset, data were also captured for the La $M_{4,5}$ edge and the Sr $L_{2,3}$ edge as well as for the low loss region to allow for deconvolution and thickness estimates.

To extract chemical information from this set of spectra, a fitting technique is used similar to that proposed by Manoubi *et al.* [43] Instead of the weighted least-squares fitting, a maximum likelihood (ML) fitting for Poisson statistics is used. The ML approach gives an unbiased estimate of the model parameters when the counting statistics are properly taken into account. This is especially important for noisy spectra like for the Sr $L_{2,3}$ edge at ≈ 2 kV, which requires long exposure times because of the extremely small inelastic cross section at these high energies. The model $F(E)$ consists of a standard background model AE^{-r} and experimental cross sections for the excitation edges.

$$F(E)=AE^{-r}+C_1M_1(E)+C_2M_2(E)+\cdots.$$

The fitting procedure results in a set of parameters, which we can use as estimates of the real parameters of the experiment. We can use the proportionality constants $C_1, C_2, \ldots$ as estimates of the chemical concentration of the different elements modeled by the experimental cross section $M_1(E), M_2(E), \ldots$. A convolution with low loss spectra to include multiple scattering is not carried out because we assume that the difference in low loss spectra is small because of the delocalization of the plasmon excitations. Recording the low loss spectra requires that the electron beam current is largely reduced to avoid overexposure of the detector and makes it difficult to position the beam on the layers with only a very weak dark field STEM image as a guide. Using convolution in the model is possible and could improve the fit, but we argue that the uncertainty in the position of the low loss spectra makes the quantification worse in this case. However, the low loss spectra enable us to estimate a thickness profile which is found to be a linear decreasing profile with a variation of less than 10% over the range of the scan ($t/\lambda \approx 0.4$ with λ the inelastic mean free path for a plasmon excitation).

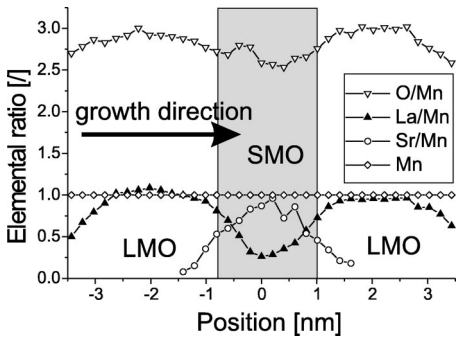

FIG. 9. Result of fitting procedure: Chemical profiles of O-*K*, La $M_{4,5}$, Sr $L_{2,3}$, and Mn $L_{2,3}$ divided by Mn $L_{2,3}$ edge signal to cancel out elastic scattering and thickness effects. Positions are calibrated from the layer to layer distance as observed in HRTEM images.

To cancel out problems with varying thickness and elastic scattering, we assume that the Mn content in the sample is constant and we divide all elemental contributions to the spectra by the Mn $L_{2,3}$ signal. The result of this process is shown in Fig. 9. The relative values in the plot are chosen to fit approximately with the nominal values in the LMO layers. This way, we circumvent most of the problems with absolute quantification by keeping only the relative quantification from place to place. We have decreased significantly the uncertainty of the different factors like thickness, absolute cross sections, multiple scattering, and elastic scattering by assuming that they have approximately the same effect on all excitation edges.

The profiles show a complementary La-Sr signal, and an oscillating O signal. The O signal drops approximately 15%, and the drop is centered around the SMO layer. The resolution and signal to noise with STEM-EELS is clearly higher as compared to the EFTEM results, but still the resolution is limited by beam broadening inside the sample, slight misorientation and/or steps in the interface plane, sample drift, and delocalization.

D. ELNES

The energy loss near edge structure (ELNES), of both the O *K* edge and the Mn $L_{2,3}$ edge are studied from the spec-

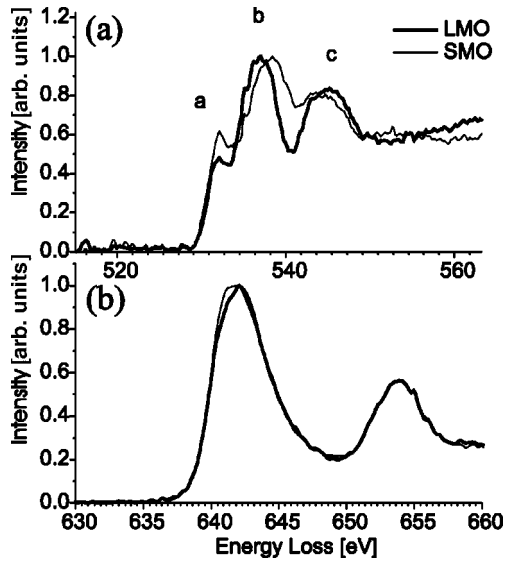

FIG. 10. ELNES from center of the layers for the O *K* edge (a) and the Mn $L_{2,3}$ edge (b).

trum of the middle of a LMO and a SMO layer, and the results are shown in Fig. 10.

1. O K-edge

The O *K* edge shows the excitation of the O 1s core state to unoccupied states near the Fermi energy. The dipole selection rules apply approximately and favor the excitation to O $2p$-like states. The actual shape of ELNES can only be compared to theoretical calculations or compared with other known compounds (fingerprinting).

Figure 10(a) shows the O K-ELNES for the center of a LMO and SMO layer. Three peaks can be distinguished and were attributed by Abbate *et al.* [4] by means of electronic structure calculations (crystal field model) to be excitations to the O $2p$ state hybridized with Mn $3d$ (a), La $5d$ or Sr $4d$ (b) and Mn $4sp$ (c). From this labeling of the peaks, we can conclude that the change of La by Sr in going from LMO to SMO, leads to an increase in the number of O $2p$ holes which are hybridized with Mn $3d$ and a shift of peak (b) by 1 eV to higher energies, indicating that the hybridized O $2p$-La $5d$ band lies about 1 eV lower in energy as the O 2p-Sr $4d$ band. Peak (a) rises by $\approx$20% in the SMO layer. Both the shift of peak (b) and the rise of peak (a) seem to be correlated, i.e., both effects follow approximately the same curve when plotted in function of position in the sample. Zampieri *et al.* [44] have shown that for bulk $CaMnO_{3-\delta}$ the oxygen deficiency decreases peak (a) of the O K-ELNES, a similar effect as seen for changing La by Sr in $La_{1-x}Sr_xMnO_3$. [4] If we extrapolate this result, we would expect that the O deficiency would have an equally important effect on peak (a) of the O K-ELNES as changing the *A* site cations. This makes it difficult to separate the effect of O deficiency from the effect of the change in *A*-site cations.

The O K-ELNES is in qualitative agreement with experimental [4,45] and theoretical [4,46] results for bulk $La_{1-x}Sr_xMnO_3$ or $La_{1-x}Ca_xMnO_3$. There is however a disagreement in the relative height of the peaks for SMO. The ELNES of $La_{0.1}Sr_{0.9}MnO_3$ in Ref. 4 shows a much stronger peak as compared to our experiments.

To our knowledge, no systematic spectroscopic study (XAS or EELS) was performed on $SrMnO_{3-\delta}$. Therefore we have to look at ''similar'' compounds to get a feeling of the behavior with varying oxygen deficiency. Zampieri *et al.* [44] have shown XAS spectra for the O K-ELNES of $CaMnO_{3-\delta}$ and a consistent drop of the prepeak with oxygen deficiency was observed. Extending this trend to SMO could explain the observed small peak (a) in the O K-ELNES of the SMO layer to be due to a significant oxygen deficiency. It should be stressed however, that this comparison is made in view of the lack of experimental data for $SrMnO_{3-\delta}$ and effects such as vacancy ordering and crystal orientation should be taken into account.

2. Mn $L_{2,3}$ edge

The Mn $L_{2,3}$ edge is shown in Fig. 10(b) and is attributed to excitations from the spin split Mn $2p$ core states to higher unoccupied states of Mn $3d$ character. The difference between the Mn $L_{2,3}$ ELNES of SMO and LMO is very small, indicating that there is almost no measured difference in the unoccupied states of Mn $3d$ character between LMO and SMO within the experimental resolution. This is highly surprising since it is assumed that the valency of Mn changes nominally from Mn^{4+} for SMO to Mn^{3+} for LMO.

Studies of ionic manganese oxides have shown that there is a significant change in the Mn $L_{2,3}$ edge, which can be correlated with the nominal Mn valency. The Mn *L* edge is expected to shift to higher energies, increase in intensity and alter the intensity ratio of the L_3 to L_2 peak with increased Mn valency. [47–49]

It can be argued that because changes can be seen in the O *K* edge, the Mn-O bonds have a considerable covalent character. The idea of hybridized Mn $3d$ and O $2p$ states is supported by experimental evidence from XPS, [7] XPS and XAS, [5] XAS (Ref. 4) and EELS. [6] A systematic study of different controlled-valency materials [3] shows that the manganites are an intermediate case between the behavior of the titanates and vanadates where the holes go to the transition metal site, and the cuprates and nickelates where holes go to the oxygen sites.

On the other hand, assuming an oxygen deficiency in the SMO layer as observed in the EELS spectra, would make the nominal valency in the SMO layer drop and thus decrease the expected difference in the Mn $L_{2,3}$ edge.

V. IMAGING SPECTROSCOPY

Figure 11 shows the results of the imaging spectroscopy technique combined to show the change of fine structure in the O *K* edge from the substrate to the layers. The waterfall plot is shown together with an intensity plot for better visibility of the position of the peaks. The three peaks in the O *K* edge fine structure are clearly discerned. A change of the fine structure can be seen as a rise of the first peak and a shift to higher energies of the second peak in the SMO layers, compared to the LMO layers. This change is

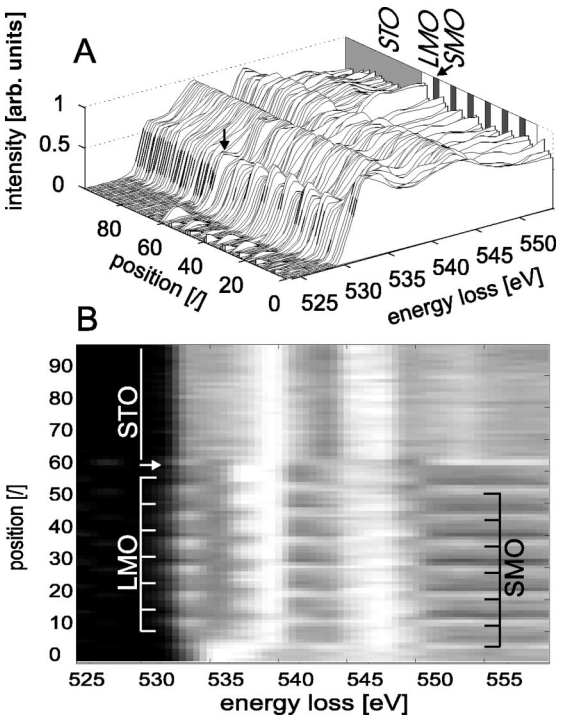

FIG. 11. Result of the imaging spectroscopy technique. ELNES of O *K* edge for substrate and layers in the LMO15SMO6 sample shown in both a waterfall plot (a) and an intensity map (b) for clarity. The arrow in (a) and (b) indicates the prepeak seen at the interface between the STO substrate and the first LMO layer.

consistent with the ELNES results obtained with STEM, but the image series technique shows the results of all the layers together. Again, the shift of peak (b) and the rise of peak (a) are correlated. Following the interpretation of the peaks of Abbate *et al.*, [4] we can conclude that O 2p holes in the SMO layers are well localized.

Note also the presence of an extra peak at the interface between the STO substrate and the first LMO layer. This prepeak is probably due to the terminating SrO layer of the substrate, connecting to a MnO_2 layer in LMO. This creates a local oxygen environment, similar to that in SMO. The result of the image series of the LMO15SMO6 sample shows similar results as in LMO9SMO4 with STEM ELNES, and shows the ELNES changes to be consistent over all layers.

VI. DISCUSSION

We will try to propose a model that combines all experimental evidence. The model can be described by the general formula $(LaMnO_3)_m(SrMnO_{3-\delta})_n/STO(100)$ for $m=9$ or 15 and $n=4$ and 6, respectively, with an estimated oxygen deficiency δ between 0.3 and 0.5. The parameters n and m are measured from counting the RHEED oscillations during the growth and checked by HRTEM and satellite spots in the ED patterns. The oxygen deficiency δ is measured from the chemical profile, obtained by fitting the experimental EELS spectra to a model, and found to be consistent with the absence of the valency effect in the $L_{2,3}$ edge.

The HRTEM images clearly show a layer-by-layer growth (as also seen on the RHEED patterns during growth [50]) of the layers with sharp interfaces between the layers. Perfect epitaxy and a distinct intensity distribution for different layers, consistent with multislice image simulations is seen. This confirms the separation of La- and Sr-containing layers while we verified with image simulation that the image is insensitive to the introduction of oxygen vacancies in the SMO layer to mimic the experimental oxygen deficiency. The model is confirmed by the chemical profiles obtained from a parametrization of the EELS spectra. A complementary La/Sr separation and an O deficiency in the SMO layer are seen when a constant Mn concentration is assumed. The hypothesis for a constant Mn concentration has been verified by noting that the intensity change in the Mn signal for both layers can be explained by preservation of elastic diffraction contrast.

The ELNES of the Mn $L_{2,3}$ edge is in agreement with the proposed model since for the estimated $0.3 \leqslant \delta \leqslant 0.5$ the nominal valency of Mn is reduced from Mn^{4+} in the direction of Mn^{3+} (pure Mn^{3+} for $\delta=0.5$). The expected changes in Mn *L* edge between LMO and the deficient SMO layer are therefore small. The fine structure inside the Mn L_3 and L_2 peak is attributed to multiplet splitting and is expected to be different for both layers, explaining the tiny difference in shape of the white lines. The O K-edge on the other hand shows a very different fine structure for both layers. Comparison with experimental results for $SrMnO_3$ shows a discrepancy in the strength of the first peak of the O *K* ELNES. Comparison with a similar compound $CaMnO_{3-\delta}$ shows that the effect of oxygen deficiency is a strong decrease in the strength of the first O K-ELNES peak. This seems to suggest that the observed ELNES for the SMO layer is likely to come from $SrMnO_{3-\delta}$ rather than $SrMnO_3$ which fits to our proposed model. The observed difference in intensity of peak (a) between LMO and SMO could be interpreted as a slight change in Mn 3d occupation and indicates that there is a small valency effect, but much smaller than expected. This is further evidence for $SrMnO_{3-\delta}$ with $\delta<0.5$.

The EFTEM results as well as the imaging spectroscopy technique agree with the STEM observations pointing out an interesting consequence. The STEM results were obtained from a mechanically polished sample, while the TEM results were obtained from a conventional ion-milled sample. The fact that both results agree so well, rules out the possible influence of sample preparation on the observed electronic structure. STEM and TEM experiments used different primary electron energies of 100 and 300 kV, giving extra support for the absence of beam damage because both results are consistent. Both samples, LMO9SMO4 and LMO15SMO6, lead to comparable observations, pointing out that apart from different scales and different total layer thickness, there is no significant difference in chemical or structural observations at the experimental accuracy.

Electronic structure calculations could further improve the interpretation of the observed ELNES peaks. The reason for the oxygen deficiency, which remarkably balances the nominal Mn valency to approximately Mn^{3+}, is related to tensile stress in the SMO layer creating oxygen vacancies.

This model can be related to the rather poor physical

properties of these type of samples as reported in Ref. 20. The absence of a large CMR effect can be attributed to the absence of strongly mixed Mn^{3+}/Mn^{4+} sites, which are thought to be essential in a double-exchange explanation of CMR.

VII. CONCLUSION

In this paper we illustrated how a combination of HR-TEM, diffraction techniques, STEM EELS, ELNES, EFTEM and imaging spectroscopy can solve nanoscale characterization problems. We investigated $(LMO)_m(SMO)_n$ heterostructures and showed that oxygen deficiency in the SMO layers leads to an adapted formula $(LaMnO_3)_m(SrMnO_{3-\delta})_n$ with $0.3 \leqslant \delta < 0.5$. This model was shown to fit all experiments and explains the poor physical properties of similar samples reported in Ref. [20]. We found chemical separation of the *A*-site cations La and Sr and the structure shows an artificial crystal with unbroken Mn lattice. The SMO layers are stabilized between two LMO layers, but tensile stress leads to oxygen vacancies increasing the number of $3d$ electrons in Mn to resemble the Mn^{3+} state of LMO. The O K-ELNES however, points out that the Mn-O bonds have a considerable covalent character and electronic structure calculations are needed to fully interpret the electronic structure of such a complex heterostructure.

ACKNOWLEDGMENTS

This work was supported by IUAP V-1 a grant of the Belgian Government. Scientific discussions, STEM time, and STEM support by J. Silcox, E. J. Kirkland, and M. Thomas are gratefully acknowledged. M. Hervieu is acknowledged for very useful solid state chemistry input. A.M. Haghiri-Gosnet is acknowledged for growing the samples.

[1] C. Rao and A. Raychaudhuri, in *Colossal Magnetoresistance, Charge Ordering and Related Properties of Manganese Oxides*, edited by C. Rao and B. Raveau (World Scientific, 1998).
[2] C. Zener, Phys. Rev. **82**, 403 (1951).
[3] M. Abbate, F.M.F. Degroot, J.C. Fuggle, A. Fujimori, Y. Tokura, Y. Fujishima, O. Strebel, M. Domke, G. Kaindl, J. Vanelp, B.T. Thole, G.A. Sawatzky, M. Sacchi, and N. Tsuda, Phys. Rev. B **44**, 5419 (1991).
[4] M. Abbate, F.M.F. Degroot, J.C. Fuggle, A. Fujimori, O. Strebel, F. Lopez, M. Domke, G. Kaindl, G.A. Sawatzky, M. Takano, Y. Takeda, H. Eisaki, and S. Uchida, Phys. Rev. B **46**, 4511 (1992).
[5] T. Saitoh, A.E. Bocquet, T. Mizokawa, H. Namatame, A. Fujimori, M. Abbate, Y. Takeda, and M. Takano, Phys. Rev. B **51**, 13942 (1995).
[6] H.L. Ju, H.C. Sohn, and K.M. Krishnan, Phys. Rev. Lett. **79**, 3230 (1997).
[7] A. Kowalczyk, A. Slebarski, A. Szajek, J. Baszynski, and A. Winiarski, J. Magn. Magn. Mater. **212**, 107 (2000).
[8] C.N.R. Rao, A.K. Cheetham, and R. Mahesh, Chem. Mater. **8**, 2421 (1996).
[9] B. Raveau, A. Maignan, C. Martin, and M. Hervieu, Chem. Mater. **10**, 2641 (1998).
[10] L.M. Rodriguez-Martinez and J.P. Attfield, Phys. Rev. B **54**, 15 622 (1996).
[11] F. Millange, V. Caignaert, B. Domenges, B. Raveau, and E. Suard, Chem. Mater. **10**, 1974 (1998).
[12] P.E. Batson, Nature (London) **366**, 727 (1993).
[13] N.D. Browning, M.F. Chisholm, and S.J. Pennycook, Nature (London) **366**, 143 (1993).
[14] P.E. Batson, J. Electron Microsc. **45**, 51 (1996).
[15] G. Duscher, N.D. Browning, and S.J. Pennycook, Phys. Status Solidi A **166**, 327 (1998).
[16] B. Rafferty and S.J. Pennycook, Ultramicroscopy **78**, 141 (1999).
[17] P.E. Batson, Ultramicroscopy **78**, 33 (1999).
[18] D.A. Muller, T. Sorsch, S. Moccio, F.H. Baumann, K. Evans-Lutterodt, and G. Timp, Nature (London) **399**, 758 (1999).
[19] A. Maignan, C. Simon, V. Caignaert, and B. Raveau, Solid State Commun. **96**, 623 (1995).
[20] P.A. Salvador, A.M. Haghiri-Gosnet, B. Mercey, M. Hervieu, and B. Raveau, Appl. Phys. Lett. **75**, 2638 (1999).
[21] B. Mercey, P.A. Salvador, W. Prellier, T.D. Doan, J. Wolfman, J.F. Hamet, M. Hervieu, and B. Raveau, J. Mater. Chem. **9**, 233 (1999).
[22] B. Mercey and J.F. Hamet, Vide: Sci., Tech. Appl. **53**, 61 (1997).
[23] M. Kawasaki, K. Takahashi, T. Maeda, R. Tsuchiya, M. Shinohara, O. Ishiyama, T. Yonezawa, M. Yosimoto, and H. Koinuma, Science **266**, 1540 (1994).
[24] P. Xu, Ph.D. thesis, Cornell, Ithaca, NY, (1991).
[25] R.F. Egerton, *Electron Energy Loss Spectroscopy in the Electron Microscope*, 2nd ed. (Plenum, New York, 1996).
[26] J.L. Lavergne, J.M. Martin, and M. Belin, Microsc. Microanal. Microstruct. **3**, 517 (1992).
[27] J. Brous, I. Fankuchen, and E. Banks, Acta Crystallogr. **6**, 67 (1953).
[28] A.M. Glazer, Acta Crystallogr., Sect. B: Struct. Crystallogr. Cryst. Chem. **28**, 3384 (1972).
[29] A.M. Glazer, Acta Crystallogr., Sect. A: Cryst. Phys., Diffr., Theor. Gen. Crystallogr. **31**, 756 (1975).
[30] P.M. Woodward, Angew. Chem. Int. Ed. Engl. **53**, 32 (1997).
[31] P.M. Woodward, Acta Crystallogr. **53**, 44 (1997).
[32] J. Topfer and J.B. Goodenough, J. Solid State Chem. **130**, 117 (1997).
[33] J. Rodriguez-Carvajal, M. Hennion, F. Moussa, and A.H. Moudden, Phys. Rev. B **57**, R3189 (1998).
[34] P. Norby, I.G.K. Andersen, E.K. Andersen, and N.H. Andersen, J. Solid State Chem. **119**, 191 (1995).
[35] J.A. Alonso, M.J. MartinezLopez, M.T. Casais, J.L. MacManus-Driscoll, P. deSilva, L.F. Cohen, and M.T. FernandezDiaz, J. Mater. Chem. **7**, 2139 (1997).
[36] J.A.M. Vanroosmalen, P. Vanvlaanderen, E.H.P. Cordfunke, W.L. Ijdo, and D.J.W. Ijdo, J. Solid State Chem. **114**, 516 (1995).
[37] B.C. Tofield and W.R. Scott, J. Solid State Chem. **10**, 183 (1974).
[38] J.F. Mitchell, D.N. Argyriou, C.D. Potter, D.G. Hinks, J.D. Jor-

gensen, and S.D. Bader, Phys. Rev. B **54**, 6172 (1996).
[39] A. Maignan, C. Michel, M. Hervieu, and B. Raveau, Solid State Commun. **101**, 277 (1997).
[40] O. Chmaissem, B. Dabrowski, S. Kolesnik, J. Mais, D.E. Brown, R. Kruk, P. Prior, B. Pyles, and J.D. Jorgensen, Phys. Rev. B **64**, 134412 (2001).
[41] T. Negas and R. Roth, J. Solid State Chem. **1**, 409 (1970).
[42] A. Berger and H. Kohl, Macromolecules **3**, 159 (1992).
[43] T. Manoubi, M. Tencé, M.G. Walls, and C. Colliex, Macromolecules **1**, 23 (1990).
[44] G. Zampieri, F. Prado, A. Caneiro, J. Briatico, M.T. Causa, M. Tovar, B. Alascio, M. Abbate, and E. Morikawa, Phys. Rev. B **58**, 3755 (1998).
[45] Y. Ju and Z. Li, Phys. Lett. A **277**, 169 (2000).
[46] S. Satpathy, Z.S. Popovic, and F.R. Vukajlovic, J. Appl. Phys. **79**, 4555 (1996).
[47] H. Kurata and C. Colliex, Phys. Rev. B **48**, 2102 (1993).
[48] J.H. Rask, B.A. Miner, and P.R. Buseck, Ultramicroscopy **21**, 321 (1987).
[49] J.H. Paterson and O.L. Krivanek, Ultramicroscopy **32**, 319 (1990).
[50] B. Mercey (private communications).